https://doi.org/10.1016/j.resconrec.2023.106893



# Recycling of red mud and flue gas residues in geopolymer aggregates (GPA) for sustainable concrete

Lan-Ping Qian[1], Muhammad Riaz Ahmad[2]**, Jian-Cong Lao[3], Jian-Guo Dai[4]*

## Highlights

- Red mud (RM) and flue gas residue (FGR) partially replaced precursor and activator
- Replacement rate of fly ash by RM and $Na_2O$ in activator by FGR reached 40% and 32%
- RM and FGR had minimal impacts on compressive strength of GPA pastes
- Concrete strength declined by 13.4% upon 100% replacement of NA by GPA

[1] Ph.D. Candidate, Department of Civil and Environmental Engineering, The Hong Kong Polytechnic University, Kowloon, Hong Kong, China. Email: lanping.qian@connect.polyu.hk

[2] Postdoctoral Fellow, Department of Civil and Environmental Engineering, The Hong Kong Polytechnic University, Kowloon, Hong Kong, China. Email: mriaz.ahmad@polyu.edu.hk (**Corresponding Author*)

[3] Research Associate, Department of Civil and Environmental Engineering, The Hong Kong Polytechnic University, Kowloon, Hong Kong, China. Email: jiancong.lao@polyu.edu.hk

[4] Professor, Department of Civil and Environmental Engineering, The Hong Kong Polytechnic University, Kowloon, Hong Kong, China. Email: cejgdai@polyu.edu.hk (**Corresponding Author*)

**Abstract**

This study proposed simultaneous utilization of red mud (RM) and flue gas residues (FGR) as a partial replacement of traditional precursors and energy-intensive activator. Reaction mechanism of geopolymer pastes were investigated through isothermal calorimetry, X-ray diffraction, thermogravimetry and infrared spectroscopy, by varying the dosage of RM (40%) and FGR (24%, 32%). Results showed that use of RM and FGR as a replacement of FA and commercial activator had a limited influence on the compressive strength. RM and FGR participated in reaction at a slower rate. After optimization, heat-cured FGR0.32 mix was selected to manufacture GPA. Engineering properties, cost analysis and environmental impact of GPA were evaluated. Natural aggregates (NA) were replaced by GPA at replacement levels of 25%, 50%, 75% and 100% by volume to prepare concrete. GPA concrete with 25% and 100% replacement level could achieve the 94.6% and 86.6% of NA concrete strength respectively at 28 days age.

**Keywords:** Geopolymer aggregates (GPA); Red mud (RM); Flue gas residues (FGR); Geopolymer aggregate concrete (GAC); Mechanical properties

## Graphical Abstract

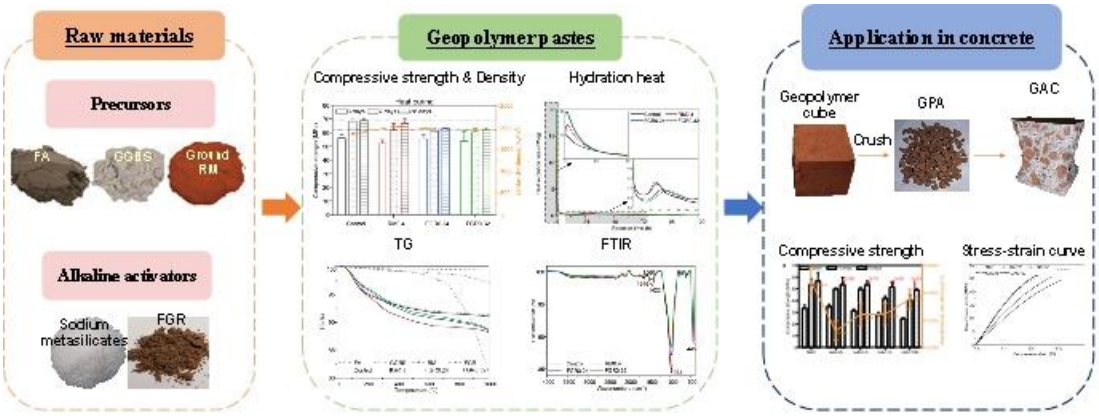

## 1 Introduction

Red mud (RM) is an industrial waste discharged during alumina extraction by Bayer process. The refining of 1 ton of alumina generates approximately 1.5-2.5 tonnes of RM [1]. The global production of RM is estimated at 70 to 120 million tonnes annually [2] due to the growing demand for alumina. China and Australia account for around 80% of total production of alumina [3]. The characteristics of RM, e.g., strong alkalinity, high fineness, and concentrated heavy metals make its reclamation further difficult [4]. The significant production of alumina has prompted a number of studies to focus on the efficient recycling of RM [5-8]. The most promising practical application of recycling RM seems to be in the construction industry which consumes a significant amount of building materials. Since RM contains Si and Al, many researchers have studied the RM-based geopolymer or alkali-activated materials which exhibited comparable mechanical characteristics and stabilization of toxic elements to other cementitious materials [9]. However, RM is not recommended as the sole precursor for preparing geopolymer due to its relatively poor reactivity and low Si/Al molar ratio, thus it is usually pretreated (e.g., alkali-thermal treatment or mechanical milling) or mixed with other Si-rich materials [10]. Furthermore, RM has been reported as the sole Na source to make low-strength blocks [11] while the $D_{50}$ (average particle size) of RM was only 3 μm, which was much finer than the values in other studies. According to the findings in [12] where the sizes of RM were under 300 μm, most of Na in the raw RM was insoluble.

Flue gas residues (FGR) refer to an industrial waste after the cleaning procedures of the flue gases generated by the incineration of municipal solid wastes, clinical wastes or sewage sludge [13]. Hong Kong has one of the world's largest sewage sludge incinerators with a design capacity of 2000 tonnes/day. Besides, the first municipal solid waste incineration plant (IWMF) with a capacity of 3000 tonnes/day is under construction in Hong Kong and will soon start to operate in 2025. It can be expected that solid wastes will increase significantly as the economy is growing and the FGR production will rise accordingly. FGR produced in the Hong Kong incineration plant contains high contents of alkaline oxides and heavy metals, posing significant

challenges to deal with this waste. FGR is mostly landfilled after stabilization/solidification with hydraulic binders (usually cement) due to its high content of heavy metals and high alkalinity. However, this is not a long-term solution due to the limited landfill capacity and wasting of recoverable resources. Few studies focused on the recycling of FGR as construction materials, e.g., sintered artificial aggregates [14, 15], blended cement [16, 17] and geopolymer [18].

Recycling wastes into artificial aggregates has been demonstrated to be an effective method of turning wastes into commercial products in the research area of green building materials [19-22]. Generally, aggregates occupy around 60% to 80% volume of concrete, hence preparing artificial aggregates from industrial wastes could significantly ease the disposal burden on landfills. Artificial aggregates currently include sintered aggregates and cold-bonded aggregates. Sintered aggregates require high temperatures over 1000 ℃ to harden the pellets by fusing raw material particles, which are energy-intensive and costly. Cold-bonded aggregates typically utilize cementitious materials to bind the waste materials at curing temperatures below 105℃. Geopolymer as a kind of cement-free binder have been reported to have good mechanical properties and superior durability [23-25]. Hence, one newly proposed type of cold-bonded aggregates is geopolymer aggregates (GPA) and it has been successfully applied in concrete or engineered composites in recent years [26-31]. Although research in the geopolymer and alkali-activated materials has sought consider attention of scientists, the raw materials utilized in this field are mostly limited to fly ash, GGBS and commercial alkaline activators. However, fly ash and GGBS are now considered as commercial products and they are slightly cheaper than cement. Besides, the greatest concern of geopolymer in terms of cost and carbon emission is the commercial alkaline activator. GPA produced in such case have higher cost and not very environmental-friendly. Hence some studies started using some low-activity wastes as precursors, whereas the quality of the produced GPA decreased [26]. Most studies of artificial aggregates focused on the pelletized aggregates but few studies explored aggregates production through crushing technology [32]. The common practice requires geopolymer concrete to be cured at elevated temperatures to achieve a reasonable strength

development rate [25]. Concrete wastes have been reported to have a more than 12% share in total solid waste in some countries [33]. A significant amount of geopolymer concrete waste can be expected in the future due to the increase in use of geopolymer concrete in construction industry. The recycled GPA as coarse aggregates have been successfully used in Portland cement concrete and geopolymer concrete [34]. Hence, the investigations on crushed GPA not only can directly recycle waste materials as GPA, but also can be a reference to the application of recycled GPA in the future.

This study aims to evaluate the feasibility of recycling both RM and FGR into synthesizing GPA. RM and FGR were designed to partially replace the main precursor and alkaline activator, respectively. Reduction of $CO_2$ emissions and cost from the commercial alkaline activator can be achieved by using FGR as a partial alkali source. In addition, replacing FA with RM is not only a timely response for the decreased supply of FA in the future but is also capable of consuming a considerable amount of RM and converting it to valuable products. FGR was selected as the waste-derived activator based on its high $Na_2O$ content from the material characterization results. Coal fly ash (FA) was the main precursor and ground granulated blast-furnace slag (GGBS) was added to improve the strength. First, the compressive strength and the reaction mechanism of the geopolymer pastes was investigated through isothermal calorimetry, X-ray diffraction (XRD), thermogravimetric analysis (TGA) and infrared spectroscopy measurement. Additionally, the leaching behavior of geopolymer pastes was also studied to evaluate if the leaching values of toxic elements are within the regulatory limits. Second, one paste mix with appropriate performance was crushed to produce GPA and then prepare concrete. The effects of different volume substitution of GPA with natural aggregates (NA) on the performance of concrete were discussed. This work is expected to provide a useful practice for large-scale recycling of RM and FGR through the manufacturing of GPA.

## 2 Materials and mix design

### 2.1 Materials

#### 2.1.1 Raw materials for geopolymer pastes and GPA

The powder materials for production of geopolymer pastes and GPA in this study included coal fly ash (FA), ground granulated blast-furnace slag (GGBS), red mud (RM) and flue gas residues (FGR). FA was locally provided by Green Island Cement Co. Ltd (Hong Kong) and GGBS was purchased from Mainland China. RM was a by-product of the bauxite refining into alumina from a plant in Henan Province, China. FGR was collected from the local sewage sludge incineration plant (T-park) in Hong Kong. In this study, some large lumps were found in the as-received RM. Hence the original RM was ground using a ball mill and then sieved to below 300 μm prior to use. From Fig. 1(a), the particle sizes of FA, GGBS and FGR were all smaller than 120 μm and the $D_{50}$ of FA, GGBS and FGR was 18.66 μm, 12.72 μm, and 6.36 μm, respectively, which were determined by a laser particle size analyzer (Malvern Mastersizer 3000). It can be found that FGR had the lowest average particle size. However, the particle sizes of RM were relatively coarser and the $D_{50}$ particle size was 47.90 μm.

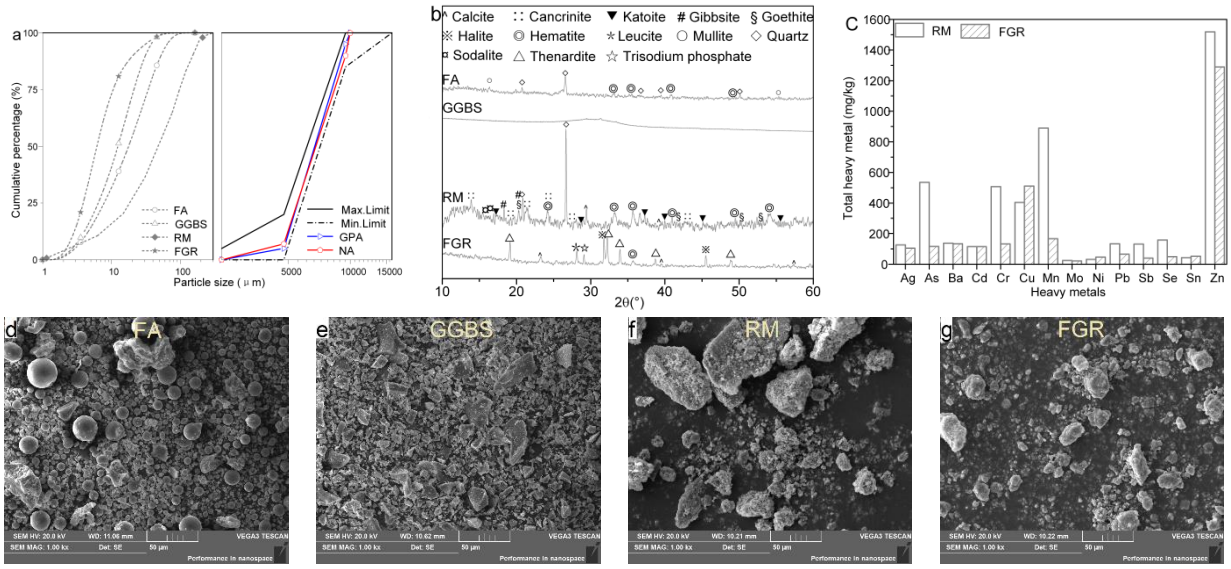


Fig. 1 Characterization of raw materials: (a) Particle size distribution of waste materials and coarse aggregates for concrete, (b) XRD pattern of waste materials, (c) Total concentration of heavy metals in RM and FGR, (d)-(g) SEM images of FA, GGBS, RM, and FGR, respectively.

Table 1 Chemical components of raw materials

| Oxides (%) | FA | GGBS | RM | FGR |
|---|---|---|---|---|
| $SiO_2$ | 49.90 | 31.80 | 17.90 | 6.80 |
| $Al_2O_3$ | 24.80 | 14.00 | 21.80 | 3.80 |
| $Fe_2O_3$ | 8.41 | 0.27 | 36.90 | 4.81 |
| CaO | 6.36 | 43.0 | 3.92 | 3.42 |
| MgO | 2.83 | 6.66 | 0.53 | 1.72 |
| $Na_2O$ | 1.84 | 1.27 | 10.20 | 38.10 |
| $K_2O$ | 1.72 | 0.41 | 0.85 | 0.56 |
| $TiO_2$ | 1.24 | 0.54 | 3.81 | 0.20 |
| $P_2O_5$ | 0.68 | 0.11 | 0.48 | 2.88 |
| $SO_3$ | 1.66 | 1.69 | 3.06 | 31.40 |
| MnO | 0.08 | 0.21 | 0.07 | 0.02 |
| Cl | 0.11 | - | - | 5.98 |
| Others | 0.38 | 0.05 | 0.47 | 0.30 |
| Specific gravity | 2.28 | 2.92 | 3.03 | 2.97 |
| Moisture content (%) | 0.20 | 0.10 | 2.91 | 0.40 |

Note: The chemical compositions were determined by Rigaku Supermini200. The specific gravity was tested by water pycnometer method following the ISO 17892-3 and moisture content was determined by drying the samples at 105 ℃ in an oven for 24 hours.

According to Table 1, as the sum content (83.1%) of $SiO_2$, $Al_2O_3$ and $Fe_2O_3$ in FA was higher than 50%, the CaO content (6.36%) was less than 18%, and the LOI value (3.33%) measured at 950 ℃ for 30 minutes was less than 6%, FA can be classified as Class F as per ASTM C618-19 [35]. The main components of GGBS were $SiO_2$ (31.8%), $Al_2O_3$ (14.0%), and CaO (43.0%). The main constituents in RM were $SiO_2$ (17.9%), $Al_2O_3$ (21.8%), $Fe_2O_3$ (36.9%) and $Na_2O$ (10.2%). The major elements in FGR were $Na_2O$ (38.1%) and $SO_3$ (31.4%). The high content of $SO_3$, which are soluble in water, highly affects the environment. Other contents such as $SiO_2$, $Al_2O_3$, $Fe_2O_3$ and CaO in FGR were low, which may indicate limited potential as precursor for geopolymerization. Besides, FA, GGBS, RM and FGR had a specific gravity of 2.28, 2.92, 3.03 and 2.97, respectively, which showed that FA was the lightest raw material of them. Additionally, the moisture contents of FA, GGBS and FGR were all less than 0.5% while the moisture content of RM was relatively higher (2.91%).

Fig. 1b presents the X-ray diffraction (XRD) patterns of the four types of powder materials. Quartz ($SiO_2$) and mullite ($3Al_2O_3$-$2SiO_2$) were the most common crystals in FA. GGBS had a

highly amorphous hump around 25-35º. RM contained many kinds of crystal phases including calcite ($CaCO_3$), cancrinite ($Na_6Ca_{1.5}Al_6Si_6O_{24}(CO_3)_{1.6}$), katoite ($Ca_3Al_2(SiO_4)(OH)_8$), gibbsite ($Al(OH)_3$), goethite (FeO(OH)), hematite ($Fe_2O_3$), quartz and sodalite ($Na_8[AlSiO_4]6Cl_2$). FGR consisted of calcite ($CaCO_3$), thenardite ($Na_2SO_4$), leucite ($KAlSi_2O_6$), hematite ($Fe_2O_3$), halite (NaCl) and trisodium phosphate ($Na_3PO_4$).

The results of total concentrations in RM and FGR are provided in Fig. 1c. The major heavy metals (>200 mg/kg) presented in RM were As (535 mg/kg), Cr (507 mg/kg), Cu (404 mg/kg), Mn (890 mg/kg) and Zn (1519 mg/kg) with the highest concentration. The major heavy metals presented in FGR were Cu (511 mg/kg) and Zn (1289 mg/kg). Other heavy metals, such as Ag, Ba, Cd, Pb, Sb and Se, were also detected in very low concentrations in RM and FGR. Hence, it is highly suggested that RM and FGR require pre-treatment when they are aimed to be recycled as construction materials.

Knowing that the morphology of phases in the final products are inherited from the parent materials, it is necessary to test the morphological patterns of these four materials through scanning electron microscopic (SEM) observed by Tescan VEGA3, as displayed in Fig. 1(d-g). Round particles were predominant in FA with several irregular fragments, which could be some impurities such as unburnt carbon. GGBS had angular-shaped particles. Majority of the RM particles were porous with irregular shape and comprised of many micrometer-sized agglomerates. Similarly, FGR particles were also irregular with fluffy appearance while the sizes were much smaller than that of RM.

Industrial-grade anhydrous sodium metasilicate ($Na_2SiO_3$-anhydrous) purchased from Qingdao Haiwan Chemical Co. Ltd, China, was employed as the alkali activator. The chemical compositions of the sodium metasilicate particles were 55.6% $Na_2O$, 43.7% $SiO_2$ and 0.7% impurities by weight, as tested by X-ray fluorescence. Therefore, the calculated silica modulus (the molar ratio of $SiO_2/Na_2O$) was 0.812 for the sodium metasilicate. The particle size range of the sodium metasilicate was between 0.3-1.0 mm with $D_{50}$ of 706 μm, as measured by a laser particle size analyzer. The solid activator particles were dissolved in tap water and cooled down

at ambient temperature before mixing with powder materials.

### 2.1.2 Materials for concrete

Type I 52.5 N OPC was locally purchased from Green Island Cement Co. Ltd (Hong Kong) as a binder to prepare concrete. River sand (＜2.36mm) with a fineness modulus of 2.70 was used as fine aggregates. The specific gravity and the loose bulk density of the river sand were 2.60 and 1495.8 kg/m$^3$, respectively. The water absorption of river sand was measured as 1.02%. The size of coarse NA (granite) was in the range of 5-10 mm. The specific gravity and the loose bulk density of the coarse NA were 2.67 and 1538.0 kg/m$^3$, respectively. The water absorption of coarse NA was measured as 0.8%. NA were washed and dried before their use in concrete. Polycarboxylate superplasticizer was adopted in mixing and tap water was used in concrete.

## 2.2 Mix design

### 2.2.1 Mix design for geopolymer pastes and GPA

The mix proportion for geopolymer pastes is provided in Table 2. The control group was the group without RM and FGR. Mass ratio of GGBS/FA (20/80) and sodium metasilicate/precursors (12%) as well as a lower water-to-binder ratio were adopted based on a previous study [32], which reported the highest compressive strength of GAC compared with other mixes. It was observed that the addition of GGBS in GPA resulted in stronger geopolymer-matrix interfaces in GAC [36]. A lower water-to-binder ratio aimed to further increase the strength. RM0.4 represented the group using RM as partial substitute of FA and 0.4 denoted the substitution rate by mass (40%). In Mix FGR0.24 and FGR0.32, 40% mass of FA was still replaced by RM and sodium metasilicate was further partially replaced by FGR. The number after FGR represented the mass replacement ratio of $Na_2O$ in sodium metasilicate by FGR (24% and 32%). The substitution rate of RM was determined by the molar ratio of $SiO_2/Al_2O_3$, which was between 3.3-4.5 as suggested in previous studies [37]. The range of molar ratio of $SiO_2/Al_2O_3$ in this study was 3.53-4.15. The replacement ratios of FGR were determined based on trial tests and overall considerations of performance and heavy metals. The powder materials were mixed first and then blended with prepared alkaline activator solution. The

199 water/precursors ratios were consistent in all mixes. A total of 48 cubes of 40 mm were mixed
200 and cast (12 cubes for each mix). The mixing of raw materials and casting of fresh pastes were
201 conducted at room temperature and a relative humidity of 65%. All paste specimens were
202 demolded 1 day after casting. To investigate the effects of curing method on the paste properties,
203 6 specimens of each group were sealed in plastic bags under ambient temperature while the
204 other 6 specimens were sealed and placed in an oven at 80°C for 24 hours (heat curing) and
205 then sealed in plastic bags till testing. The optimal mix balancing the utilization ratios of RM
206 and FGR as well as the performance assessment was selected for the GPA manufacturing. The
207 crushing technique was employed as the production method of GPA referring to a previous
208 study [32].

209 Table 2 Mix proportions of geopolymer paste and concrete (kg/m$^3$)

| **Geopolymer paste mix** | **GGBS** | **FA** | **RM** | **FGR** | **Sodium metasilicate** | **Water** |
|---|---|---|---|---|---|---|
| Control | 300 | 1200 | n/a | n/a | 180 | 417 |
| RM0.4 | 300 | 720 | 480 | n/a | 180 | 417 |
| FGR0.24 | 300 | 720 | 480 | 63 | 136.8 | 417 |
| FGR0.32 | 300 | 720 | 480 | 84 | 122.4 | 417 |
| **Concrete group** | **Cement** | **Sand** | **GPA** | **NA** | **Water** | **Superplasticizer** (in solid) |
| NAC | 420 | 756 | n/a | 1069 | 168 | 2.1 |
| GAC25 | 420 | 756 | 200 | 802 | 168 | 2.1 |
| GAC50 | 420 | 756 | 400 | 535 | 168 | 2.1 |
| GAC75 | 420 | 756 | 600 | 267 | 168 | 2.1 |
| GAC100 | 420 | 756 | 800 | n/a | 168 | 2.1 |

210 **2.2.2 Mix design for concrete**

211 The NA and crushed GPA of 5-10 mm size were employed in the preparation of concrete. As
212 shown in Table 2, five concrete groups were cast in total. The control group was prepared by
213 using NA and designated as NAC. The other four groups were geopolymer aggregate concrete
214 (GAC) incorporating 25%, 50%, 75% and 100% GPA by volume, respectively. The mass of
215 GPA was calculated based on the saturated-surface-dried (SSD) particle density (Section 3.2.1
216 and Section 4.2). Considering its high water absorption, GPA were pre-saturated and sealed
217 prior to use. The mixing and casting of concrete were conducted at the same temperature and

relative humidity with that of geopolymer. For each group, nine cylindrical specimens were cast in total to test the mechanical properties at the curing age of 3, 7 and 28 days. The diameter and height of the cylindrical specimen were 75 mm and 150 mm, respectively. All the concrete specimens were demolded 1 day after casting and cured in lime water till the testing day.

## 3 Testing procedures

### 3.1 Test methods for geopolymer pastes

#### 3.1.1 Density and Compressive strength

To understand the strength development, the unconfined compressive strength (UCS) of paste cubes was tested at 3, 7 and 28 days, respectively. For each group of geopolymer paste, six samples were used to test the density through the Archimedes method in water. Then these samples were dried and tested under compression at a loading rate of 0.6 MPa/s in accordance with ASTM C109/C109M [38]. The density and UCS reported in this study were the average values of six specimens.

#### 3.1.2 Isothermal calorimetry

Isothermal calorimetry was used to measure the hydration heat of four geopolymer paste groups according to ASTM C1679 [38]. To figure out the role of RM and FGR, the test was continued for 120 hours. Due to the equipment limitation, mixing could only be conducted outside the instrument and the mixed pastes were then quickly introduced into the calorimeter. The starting time on the plots represented the time when the samples were placed in the instrument, which was around 2 minutes after the start of mixing.

#### 3.1.3 XRD test

The broken pieces of the heat-cured geopolymer pastes after compression test at 28 days were immersed in isopropanol for 7 days to stop further hydration of pastes. After that samples were dried in a vacuum freezer for 6 hours. The dried fractions were ground into powder form with sizes less than 45 μm using a mortar and pestle. The equipment used in the XRD test for both waste materials and geopolymer pastes was Rigaku SmartLab 9kW-Advance. The XRD test

was conducted in a 2θ range from 10° to 60° with a scanning step of 0.02°.

### 3.1.4 Thermogravimetric analysis

The sample preparation for Thermogravimetric analysis (TGA) test was the same as that for XRD. A dried powder sample (around 10 mg) with particle size under 45 μm was used for each mix. TGA was performed using Rigaku Thermo Plus EVO2 and the temperature was gradually increased from 30°C to 1000 °C with a heating rate of 10°C/min.

### 3.1.5 Infrared spectroscopy measurement

The sample preparation method for Fourier Transform Infrared Reflection (FTIR) test was the same as that for XRD and TGA. Around 5 mg dried powder with size under 45 μm was tested for each mix. In this study, a Bruker Tensor Π spectrometer was used to conduct the FTIR test. The scanning was conducted by Attuned Total Reflection (ATR) method in the range of wavenumbers from 400 to 4000 $cm^{-1}$ with a resolution of 4 $cm^{-1}$.

### 3.1.6 Heavy metal tests

Raw RM and FGR were digested through aqua-regia digestion and the total heavy metal concentration was detected using the Inductively Coupled Plasma-Optical Emission Spectrometer (ICP-OES).

The leaching test was performed on raw RM and FGR as well as four heat-cured geopolymer pastes. The paste samples were crushed to a size range under 4 mm and dried at 105 °C. Two different leaching methods were used to investigate and compare the leaching behavior. One leaching test was the toxicity characteristic leaching procedure (TCLP) in line with US EPA Method 1311 [39]. The other test was the synthetic precipitation leaching procedure (SPLP) according to the US EPA Method 1312 [40]. The difference between these two tests was only the extraction liquid used. The TCLP test generally aims to examine the feasibility for soil landfilling or remediation while the SPLP test explores the leaching behavior in simulated acid rain. Liquid after leaching tests was filtered through the 0.45 $\mu$m glass fiber filter and then digested by nitric acid. The detailed procedures of these tests can be found in previous studies

[18, 41]. The leaching concentrations were also determined by the ICP-OES.

### 3.2 Test methods of GPA

#### 3.2.1 Shape index, particle density and water absorption

The shape index was tested as per BS EN 933-4 [42]. Approximately 1500 g GPA with the diameter between 5 mm and 10 mm were soaked in water for 24 hours, then taken out and wiped with a dry towel to SSD condition. The mass of SSD GPA was denoted as $m_1$. After that, the GPA were put into a measuring glass bottle. Next, water was carefully poured into the bottle until no bubbles were found between the water surface and a glass cover. The total weight of the water, GPA, bottle and glass cover was recorded as $m_2$. The weight of the bottle filled with water as well as the glass cover was marked as $m_4$. The measured GPA were taken out and dried in an oven at 105℃ until no further mass loss was observed. The mass of the oven-dried GPA was $m_3$. The oven-dried particle density $\rho_{OD}$ (unit: kg/m$^3$) can be calculated according to **Eq. (1)**, as follows:

$$\rho_{OD} = \frac{m_3}{m_1 - (m_2 - m_4)} \times 1000 \quad \textbf{(1)}$$

Additionally, the water absorption $WA$ of the crushed GPA can be calculated by **Eq. (2)**:

$$WA = \frac{m_1 - m_3}{m_3} \times 100\% \quad \textbf{(2)}$$

Based on the oven-dried particle density and water absorption of GPA, the calculation of SSD particle density $\rho_{SSD}$ is shown in **Eq. (3)**:

$$\rho_{SSD} = (1 + WA)\rho_{OD} \quad \textbf{(3)}$$

#### 3.2.2 Bulk crushing strength

The bulk crushing strength of GPA was determined in accordance with GB/T 17431.2-2010 [43], which was similar to the method in EN 13055:2016 [44]. A steel cylinder container with an inner bottom area of 10000 mm$^2$ and inner height of 100 mm was used. A circular loading head with the same area of 10000 mm$^2$ was placed on the top of leveled GPA surface. A

compression load was applied with a loading rate of 0.3 kN/s until the compression of GPA reached 20 mm from the top surface. The ultimate load was recorded as $F_1$ (unit: N). The bulk crushing strength (σ) of GPA (unit: MPa) was calculated by **Eq. (4).**

$$\sigma = \frac{F_1 + F_2}{A} \quad \textbf{(4)}$$

where $F_2$ was the gravity of the loading head (unit: N), which was 17 N in this test; and A was the inner area of the cylinder container (10000 $mm^2$).

### 3.3 Test methods of GAC

#### 3.3.1 Workability, density and compressive behavior

After mixing, the slump of concrete was tested and the value was taken as the nearest 5 mm, according to BS EN 12350-2 [45]. The strength development of GAC was studied by testing the UCS of GAC samples at 3, 7 and 28 days, respectively. Before the compressive test, the density at 28 days was measured first by the Archimedes method. The compressive test followed the ASTM C39/C39M-20 [46]. The elastic modulus test was performed at the age of 28 days according to ASTM C469/C469M-14 [47]. For the elastic modulus test, surface capping by gypsum on the top and bottom was performed for all the cylinder specimens. Three longitudinal strain gauges were fixed on each specimen with a length of 5 mm to measure the strain. During the test, the loading rate was set as 0.6 MPa/s.

#### 3.3.2 Microstructure characterization

Some crushed fragments after the compressive strength were collected and further reduced into small pieces of 4-8 mm in size, where the aggregate-matrix interface could be observed. Samples were immersed into isopropanol for 7 days to stop the hydration process and then dried in vacuum freezer. Then, the samples were embedded into fresh epoxy resin and vacuumed to remove the air bubbles. After the setting of epoxy resin, the samples were polished to a smooth surface as explained in the author's previous study [18], and coated with the gold sputter. The micromorphology and element distribution of the aggregate-matrix interface was investigated by Tescan VEGA3 with an energy dispersive X-ray spectroscopy (EDS) detector.

# 4 Results

## 4.1 Geopolymer Paste

### 4.1.1 Density and compressive strength

Fig. 2a and Fig. 2b depict the UCS of the synthesized geopolymer pastes under ambient and heat curing conditions, respectively. For ambient-cured samples, all four groups had a comparable UCS at 28 days. However, for heat-cured samples, the control group obtained the highest UCS (68.82 MPa) at 28 days and RM0.4 obtained slightly (3%) lower strength compared with the control group. The UCS of heat-cured FGR0.24 and FGR0.32 further decreased by 5.3% and 7.0% respectively compared with heat-cured RM0.4. Under ambient curing, FA, RM and FGR dissolved slowly at the early age and the dissolution increased with the curing time, which explained the comparable UCS to the control group at 28 days. However, under heat curing, more FA particles may be activated because of higher amorphous degree in FA than RM. The potential of FA was stimulated under heat curing and the differences between the RM-included samples and the control group were enlarged. It can also be found that the difference in UCS between the two FGR included samples was marginal. It was also observed that the UCS of heat-cured samples were higher than their corresponding ambient-cured ones at all curing ages. This has been commonly reported for geopolymer materials because high temperature could accelerate the reaction degree at the early age [48-50]. In addition, the UCS of ambient-cured pastes substantially increased with the curing time while the UCS of heat-cured pastes could achieve 75%-90% at 3 days of their 28-day UCS and the followed strength development was marginal.

Fig. 2a and Fig. 2b also show the 28-day dry density of all four groups under ambient curing and heat curing, respectively. The RM0.4 group had the largest density among the four groups regardless of curing condition due to the highest specific gravity of RM. Meantime, the control group had the lightest density due to the smallest specific gravity of FA. Compared with RM0.4, the density of FGR0.24 and FGR0.32 decreased with the addition of FGR. The reason may be that sodium metasilicate was completely dissolved in water before mixing with precursors

while the FGR particles occupied the volume at the beginning while dissolved and reacted at later curing time. However, the initial space that FGR particles originally occupied remained, hence the density was found to be decreased. Besides, another reason could be that the total percentage of FGR and sodium metasilicate in the FGR-added groups (13.32% in FGR0.24 and 13.76% in FGR0.32) was slightly higher than that in RM0.4 group (12%) as listed in the mix proportions (Table 2).

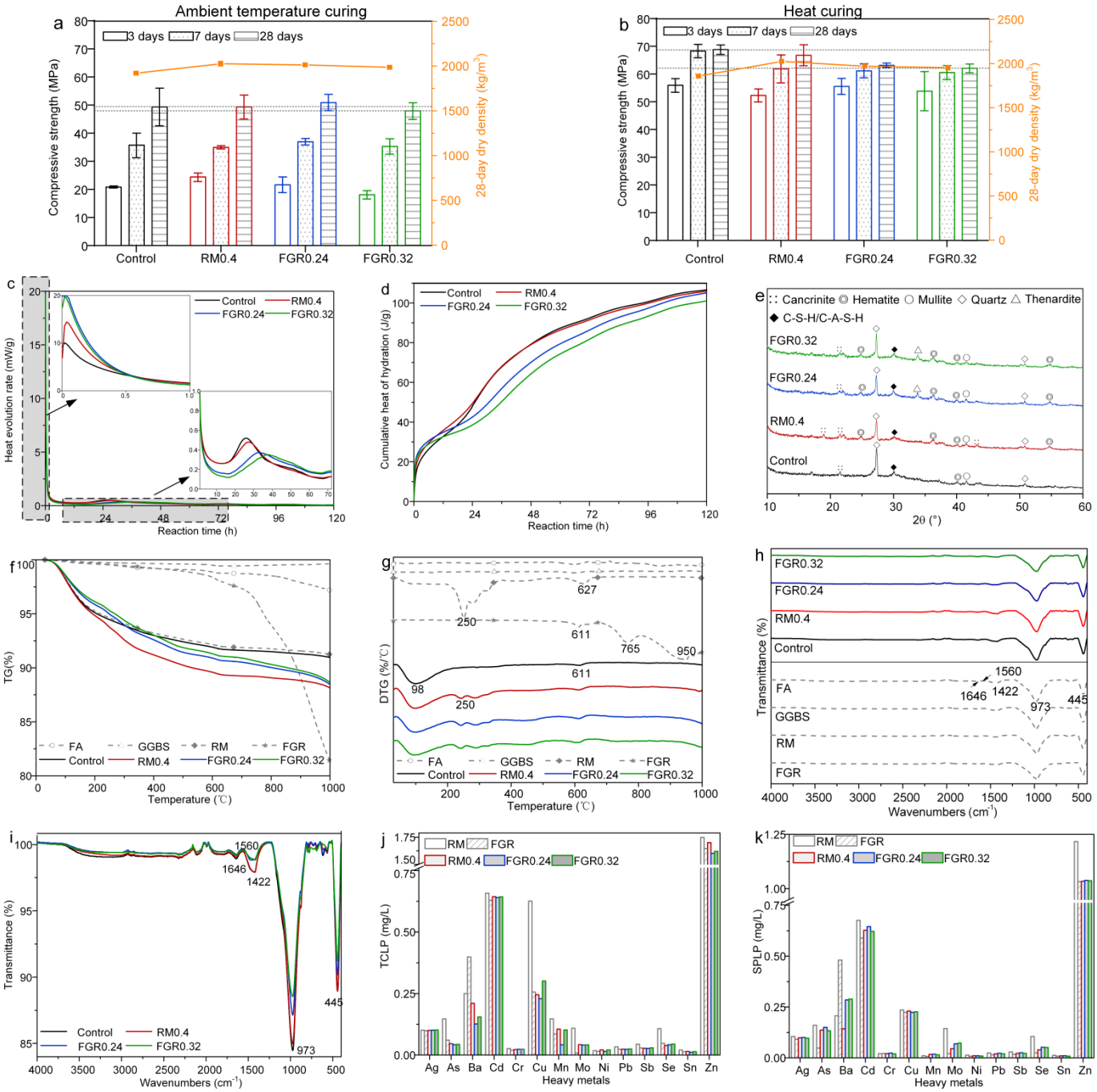

Fig. 2 Compressive strength and dry density of geopolymer pastes at 28 days: (a) Ambient temperature curing, (b) Heat curing, (c) Heat rate of evolution and (d) Cumulative heat release of geopolymer pastes, (e) XRD patterns of geopolymer pastes, (f) TG analysis and (g) DTG analysis of raw materials and geopolymer pastes, (h) FTIR of raw materials and geopolymer pastes and (i) Enlarged FTIR curves for geopolymer pastes, Leachability of heavy metals from raw materials and geopolymer pastes (j) TCLP and (k) SPLP. (XRD, TGA, FTIR and leaching tests were only performed for the heat-cured samples)

#### 4.1.2 Heat of evolution

The heat evolution rate and the cumulative heat during the first 120 hours were recorded as presented in Fig. 2c and Fig. 2d, respectively. All the results were normalized to the thermal power per gram of total precursors. In Fig. 2c, the first exothermic peak within the first hour was attributed to the wetting and chemical dissolution of the precursors and the precipitation of the dissolved silicate-aluminate. It was evident that the three RM-contained groups had higher peak intensity than the control group. This was also observed in previous studies [51], which was explained by a higher solubility of $Al_2O_3$, $SiO_2$ and CaO in a higher NaOH concentration due to the high alkalinity of RM. With further replacement by FGR, the two FGR-added groups presented higher peak values. This was because the wetting and dissolution of FGR released more heat. Accordingly, at the beginning stage the cumulative heat release amount of the control sample was the lowest (Fig. 2d).

The second peak, which also occurred commonly in geopolymer materials, was due to the nucleation, growth, and precipitation of reaction products. Compared to the other three groups, the second peak of the control group was the highest and its peak crest was also the earliest. RM0.4 had the second highest and earliest peak. This phenomenon may be explained by that RM reacted slower than FA, which was consistent with the above analysis for UCS results. While the FGR-added groups had delayed and the lowest peak intensities, which can be associated with the fact that a part of $Na_2O$ in FGR was not able to participate in the reaction at the early stage. Moreover, the presence of impurities and heavy metals can also slow down the reaction of FGR in the geopolymer system. As a result, the total heat of the control group was the highest while the total heat of the RM0.4 was the second highest. The total heat of FGR0.32 was the lowest among all pastes and this trend was also consistent with the UCS results at 28

379 days.

380 **4.1.3 XRD patterns**

381 The phases in the geopolymer samples were characterized by XRD analysis and the results are
382 displayed in Fig. 2e. For simplicity, only the heat-cured samples were analyzed in the following
383 sections in this study. The XRD pattern of the control group showed peaks such as hematite,
384 mullite, quartz, which were unreacted phases inherited from raw FA. Besides, the hump peak
385 around 29.5° indicated the co-existence of poorly disordered C-S-H gels and calcite crystals
386 due to the high content of CaO in GGBS [32]. It should be mentioned that the geopolymer gel
387 was hard to identify through the XRD pattern due to its amorphous nature and coexistence with
388 the other crystalline phases [52], however, the existence of geopolymer gel will be shown in
389 the following sections. By comparing with the XRD patterns of FA and GGBS in Fig. 1b, a new
390 crystalline phase namely cancrinite was identified, which has also been reported in the literature
391 and was related to geopolymer paste [53].

392 For XRD patterns of samples with RM or FGR, the identified peak numbers were much lesser
393 than those in raw RM and FGR as shown in Fig. 1b. Some phase peaks declined significantly
394 such as quartz compared with raw RM. This can be associated with the reaction of some phases
395 in RM and FGR under a highly alkaline environment. Compared with the control group, the
396 number of hematite peaks was more in the three RM-added groups. It is interesting to mention
397 that the three RM-added groups had no significant differences, which revealed that the FGR
398 could effectively serve as an activator in this study. In addition, thenardite was found in the two
399 FGR-included groups, which could act as weak alkaline activators as reported in previous
400 research [54]. These XRD results agreed with the UCS results.

401 **4.1.4 Thermogravimetric analysis**

402 The thermal stability of raw materials and geopolymer pastes was analyzed by the thermal
403 gravimetry (TG) and derivative thermal gravimetry (DTG) curves as displayed in Fig. 2(f-g).
404 The mass loss values for GGBS and FA from 30°C to 1000°C were only 0.38% and 2.81%,
405 respectively. Similar mass loss values were reported in literature [55, 56]. The mass loss for

406 RM from 30°C to 1000°C was higher (8.75%). Similar amounts of mass loss were also observed
407 in recent studies [8]. The mass loss of RM was initiated from the beginning of heating. DTG
408 curve of RM showed two main distinct peaks around 250°C and 627°C. The DTG peak around
409 250°C corresponded to gibbsite and goethite [57, 58], which were also confirmed in XRD
410 patterns. The DTG peak between 600-900°C was due to the release of $CO_2$ during the
411 breakdown of calcite. The mass loss of FGR was the highest (18.61%), which was similar to
412 the values reported in previous research [59, 60]. The mass of FGR was quite stable up to 600°C
413 and a sharp decrease was observed beyond that. DTG curve of raw-FGR showed three distinct
414 peaks around 611°C, 765°C and 950°C. The first and second DTG peak was due to the
415 decomposition of calcite. The third peak may be attributed to the melting and evaporation of
416 soluble complex Na, K and Cl salts as well as the decomposition of the sulfate phases [60].

417 From Fig. 2f, it is evident that the total mass loss of the control group was the lowest (9.04%)
418 and the loss of RM0.4 was the highest (11.83%). The mass losses of two FGR-added samples
419 were similar to the RM0.4 samples (FGR0.24: 11.52%; FGR0.32: 11.32%). The reason will be
420 explained after the illustration of DTG curves. From Fig. 2g, a broad peak between 30 ℃ and
421 180 ℃ was distinct in all the geopolymer paste, which indicated the evaporation of free water
422 initially at lower temperatures and physically bound water at higher temperature up to 180°C
423 [61, 62]. The control sample and the RM0.4 sample had a comparable rate of mass loss between
424 30 ℃ and 180 ℃ and slightly higher than the two FGR-added samples, which was in line with
425 the trend of UCS. At around 611°C, a small peak representing the decomposition of calcite
426 appeared in all four groups. Except for the control group, all the other three groups exhibited
427 similar trends and had a peak around 250 ℃, which was due to the gibbsite and goethite in RM.
428 It is interesting to mention that this peak intensity was smaller than that of the raw RM. On one
429 hand, it was because the coexistence of other raw materials reduced the intensity. On the other
430 hand, part of RM particles reacted. This also explained the highest mass loss of RM0.4 sample.
431 It is important to mention that not all the DTA peaks of raw FGR were present in the FGR-
432 added geopolymers, which could be associated with the high reaction degree of FGR in the
433 geopolymer. The nearly complete reaction of FGR could explain the similar mass loss compared

434 with RM0.4.

435 **4.1.5 Infrared Spectroscopy**

436 All FTIR curves for raw materials and geopolymer pastes are displayed in Fig. 2h. The FTIR
437 curves of four geopolymer pastes are enlarged in Fig. 2i for clearer illustration. Two wavelength
438 bands related to the tetrahedral $AlO_4$ and $SiO_4$ groups were observed in both FA and GGBS
439 (447 $cm^{-1}$ and 1054 $cm^{-1}$ in FA; 495 $cm^{-1}$ and 911 $cm^{-1}$ in GGBS). The shift of the larger band
440 was attributed to the higher amorphous phase in GGBS [63]. Two typical bands in the RM were
441 observed at 984 $cm^{-1}$ and 433 $cm^{-1}$ which were identified as quartz and hematite phases [64].
442 Three major bands in the FGR were found at 1110 $cm^{-1}$, 615 $cm^{-1}$ and 450 $cm^{-1}$, which were
443 linked to the stretching and bending vibration of $SO_4$ group [18].

444 For the control sample, characteristic bands detected at ~973 $cm^{-1}$ corresponded to Si–O-T (T:
445 tetrahedral Al or Si) and peak at ~445 $cm^{-1}$ was associated with the bending vibration of Si-O-
446 Al [65]. These peaks were associated with the presence of geopolymer products and their
447 intensities revealed the degree of geopolymerization, which confirmed a similar
448 geopolymerization degree in the control sample and RM0.4 sample while the lower degree in
449 the two FGR-added samples. The absorption bands at ~1422 $cm^{-1}$ corresponded to stretching
450 vibration of C-O which reflected the presence of carbonate in geopolymer. The two FGR-added
451 groups had lower intensities at this band, which indicated the less carbonate products. The broad
452 bands between 3680 $cm^{-1}$ and 3000 $cm^{-1}$ as well as a weak absorption peak at ~1646 $cm^{-1}$ were
453 due to the stretching vibration of O-H bond and H-O-H bending vibrations of interlayer
454 adsorbed water, respectively [66]. The peaks in the FTIR curves of raw FA, GGBS and RM
455 were not obvious in the curves of geopolymer pastes because these peaks were close to the
456 peaks of geopolymer products. For the samples containing FGR, peaks around 1110 $cm^{-1}$ and
457 615 $cm^{-1}$ present in raw FGR were also not found due to its participation in the
458 geopolymerization.

459 **4.1.6 Heavy metal leaching**

460 Leaching concentrations of different heavy metals determined from TCLP and SPLP methods

461 are provided in Fig. 2(j-k). It should be mentioned that all the leached values of all geopolymer
462 samples were lower or similar to that of raw FGR. However, the concentrations of leached
463 heavy metals from all the paste samples by TCLP and SPLP tests were far below the regulatory
464 limits advised by the EPA TCLP regulatory limits (Ag, As, Cr, Pb, and Cr: 5 mg/L; Cd: 1 mg/L)
465 [67]. GPA were designed to be used in concrete and the leached values are expected to be further
466 reduced significantly, when GPA is encapsulated inside concrete. The leached values of
467 geopolymer samples incorporating RM were reduced compared with the raw RM samples. This
468 indicated that geopolymer shows high immobilization efficiency for the RM waste as compared
469 to FGR [68].

470 **4.2 GPA**

471 **4.2.1 GPA properties**

472 From the UCS results of geopolymer pastes in Section 4.1, FGR0.32 group utilized the highest
473 amounts of waste materials (RM and FGR) while maintaining a slightly lower UCS compared
474 to the other three samples. Besides, the heat-cured samples obtained higher strength than their
475 corresponding ambient-cured samples. As demonstrated by previous studies, early heat curing
476 was effective to mitigate the shrinkage problem of geopolymer [69, 70]. Therefore, the heat-
477 cured FGR0.32 mix was selected to manufacture the GPA. The cubic paste specimens were
478 crushed into GPA before heat curing to minimize the crushing energy for GPA production. The
479 heat curing condition for GPA was the same as that for the pastes. According to the UCS results,
480 the 7-day UCS of heat-cured FGR0.32 could reach 97% of their 28-day UCS, hence the crushed
481 GPA at 7 days were used for casting concrete. The bulk crushing strength of GPA and NA was
482 measured as 9.2 MPa and 13.6 MPa, respectively. The strength of GPA in this study was higher
483 than that of most cold-bonded artificial aggregates in literature as displayed in Table S1. This
484 was due to their different raw materials, mix proportions and curing conditions. Moreover, as
485 indicated by Table S1, a smaller aggregate size range could lead to a higher bulk crushing
486 strength due to size effect and more flaws in bigger particles [71, 72]. The particle size
487 distributions of GPA and NA in this study meet the grading requirements in GB/T 17431.2-

2010 [43] as shown in Fig. 1a. A slightly smaller shape index of GPA (2.05) than that of NA (2.12) was found. The average values of oven-dried particle density and water absorption of the GPA were measured to be 1620.5 kg/m$^3$ and 24.38%, respectively, which were also similar to those values in Table S1. According to **Eq. (3)**, the SSD particle density was calculated as 2015.6 kg/m$^3$.

### 4.2.2 Cost and carbon emissions of GPA

The material cost and carbon emissions of GPA in this study were calculated as listed in Table 3. All of the material costs and carbon emissions are provided based on the laboratory supply list and previous research [32]. Two types of GPA with the best mechanical performances [GPA1 and GPA2] or another two types of GPA with the highest waste utilization [GPA3 and GPA4] were selected as references. Here the use of RM, FGR and incineration bottom ash were assumed to require zero cost and generate zero carbon footprint because it consumes hazardous solid waste that brings a positive effect on the environment. The results showed that the GPA in this study have the lowest cost (465.0 HKD/metric ton) and carbon emission (0.122 kg$CO_2$e/kg) among the four types of GPA mainly due to the decreased dosage of commercial activator. The greatest concern of geopolymer in terms of cost and environment is the activator. However, this issue can be mitigated in this study because the use of FGR can reduce the commercial activator dosage up to 32%. Moreover, the cost and carbon emission of GPA was normalized by the cubic compressive strength of their pastes. Obviously, the cost and embodied carbon per MPa of GPA in this study were also the lowest benefitted by the highest cubic strength of pastes. The current price of NA is around 160 HKD/metric ton in the market. The carbon emission of the crushing processes for NA was around 0.00618 kg$CO_2$e/kg [73]. However, the crushing energy of GPA is lower than that of NA due to the their lower compressive strength when being crushed, hence resulting in lower carbon emissions. The cost and carbon emission for the heat curing were estimated based on the energy consumption [73] and the result was 849.6 HKD/metric ton and 0.164 kg$CO_2$e/kg, respectively. However, this part of energy could be replaced by the waste heat from incineration plants. Besides, heat curing could improve the production efficiency, thus compensating the cost and emissions.

**Table 3** Costs and carbon emissions of GPA

| Raw Materials | Cost (HKD/metric ton) | Embodied carbon ($kgCO_2e/kg$) | GPA Mix Proportion (metric ton) | | | | |
|---|---|---|---|---|---|---|---|
| | | | GPA0 (This study) | GPA1 [32] | GPA2 [32] | GPA3 [73] | GPA4 [73] |
| FA | 400 | 0.008 | 0.3391 | 0.6849 | 0.5634 | 0.5929 | 0.5714 |
| GGBS | 450 | 0.083 | 0.1412 | - | 0.1408 | 0.1071 | 0.1071 |
| RM | 0 | 0 | 0.2260 | - | - | - | - |
| FGR | 0 | 0 | 0.0396 | - | - | - | - |
| Incineration bottom ash | 0 | 0 | - | - | - | 0.0143 | 0.0357 |
| $Na_2SiO_3$-Anhydrous | 4600 | 1.860 | 0.0576 | 0.1096 | 0.0845 | 0.0714 | 0.0714 |
| Water | 4.5 | 0.001 | 0.1964 | 0.2055 | 0.2113 | 0.2143 | 0.2143 |
| GPA Cost (HKD/metric ton) | - | - | 465.0 | 776.3 | 678.4 | 614.75 | 606.16 |
| GPA Embodied carbon ($kgCO_2e/kg$) | - | - | 0.122 | 0.210 | 0.174 | 0.147 | 0.146 |
| Cubic Strength (MPa) | - | - | 62.1 | 62.2 | 57.3 | 44.5 | 36.4 |
| GPA cost per MPa (HKD/metric ton/MPa) | - | - | 7.49 | 12.48 | 11.84 | 13.81 | 16.65 |
| GPA embodied carbon per MPa ($kgCO_2e/kg/MPa$) | | | 0.0019 | 0.0034 | 0.0030 | 0.0033 | 0.0040 |

## 4.3 GAC

### 4.3.1 Slump, density and Compressive Strength

The slump of NAC, GAC25, GAC50, GAC75 and GAC100 was measured as 150, 155, 160, 170 and 180 mm, respectively, which met the requirements of flowability [45]. The slump increase with the volume of GPA was due to the lighter density of GPA. The UCS development and strength/density ratio at 28 days as well as the stress-strain curves of GAC are plotted in Fig. 3a and Fig. 3b, respectively. The 28-day density of GAC reduced from 2413 to 2082 $kg/m^3$ with the increased replacement level of GPA from 0% to 100% due to the lightweight feature of GPA. The maximum reduction of density reached 13.7% compared with NAC. It can be

observed from Fig. 3a that although the strength/density ratios of all GAC groups were lower than that of NAC, the strength/density ratio was increased with the replacement ratio of GPA. The strength/density ratio ($23.9\times10^{-3}$ MPa $m^3$/kg) of GAC100 in this study was slightly higher than the highest ratio ($22.7\times10^{-3}$ MPa $m^3$/kg) in previous GAC research according to a recent review [26, 32]. The incorporation of GPA decreased the concrete strength. The decrease in strength was only 5.4% and 5.7% at 25% and 50% replacement levels, respectively. However, a slightly higher reduction in strength was observed for the 75% and 100% replacement level which was 9.4% and 13.4%, respectively. It was also reported in past studies that artificial aggregates could reduce concrete strength [74]. As can be seen from Fig. 3b, the elastic modulus of GAC25 and GAC50 was similar to that of NAC (31.4 GPa). However, the elastic modulus of GAC75 and GAC100 decreased to 23.8 GPa (24.2% reduction) and 19.2 GPa (38.9% reduction), respectively. The reduction of elastic modulus was attributed to the lower elastic modulus of GPA compared with NA [74].

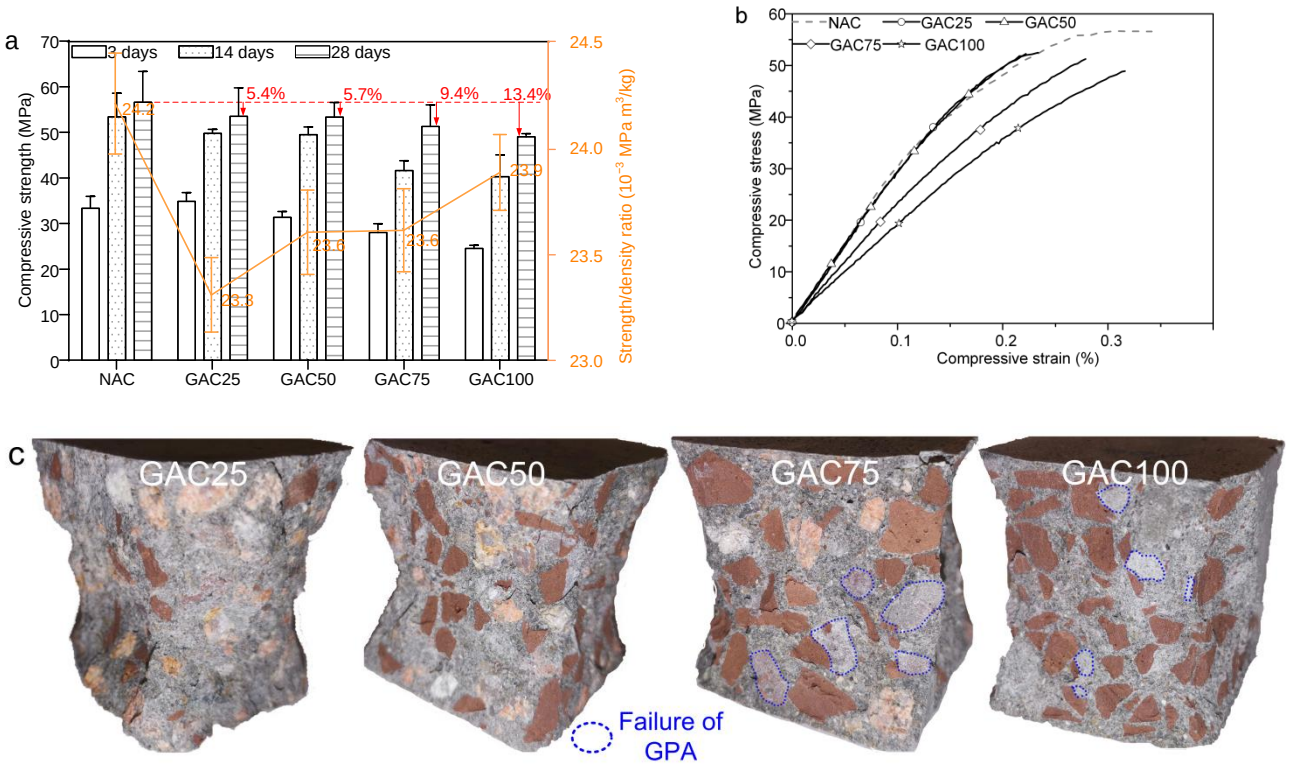

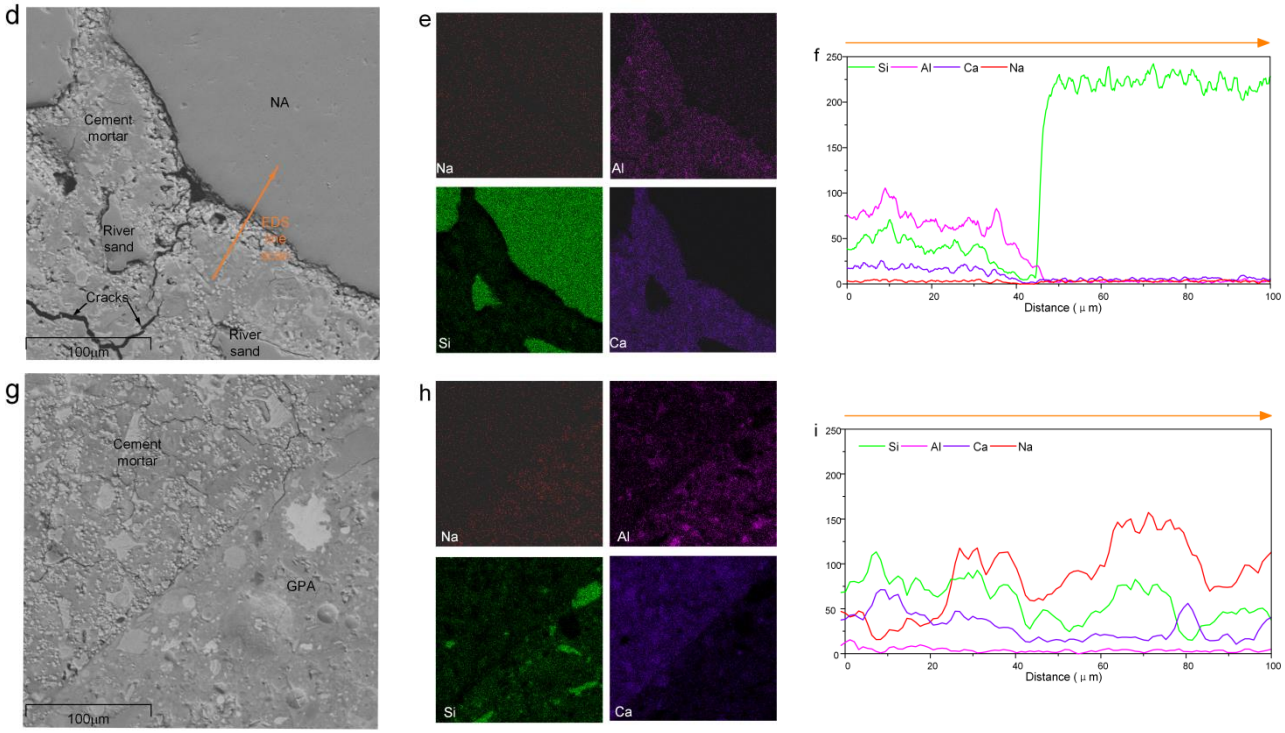


539 Fig. 3 (a) Compressive strength development and strength/density ratio, (b) Stress-strain curves
540 of concrete, (c) Failure mode of GAC, (d)-(f): BSE image of NA-matrix interface, elemental
541 mapping and EDS line scanning, respectively, (g-i): BSE image of GPA-matrix interface,
542 elemental mapping and EDS line scanning, respectively.

543 Fig. 3c displays the failure modes of four GAC groups. Generally, interface failure is common
544 for NAC, and hence such failure mode is not shown here. For artificial aggregate concrete,
545 aggregate failure was considered as the primary failure mode [32]. However, the combination
546 of interface failure and aggregate failure was observed for the GAC as marked by the blue
547 dotted circles. Such interface failure in GAC was more evident in GAC75 and GAC100, which
548 indicated that the strength of partial GPA was higher than that of surrounding cement mortar.

549 **4.3.2 Microstructure analysis**

550 The aggregate-matrix interfaces between GPA or NA and cement mortar were further
551 investigated by microscopic analysis in the Backscattered-Electron (BSE) mode and element
552 mapping as shown in Fig. 3(d-e) or Fig. 3(g-h). EDS line scan was also conducted at the
553 interface (along an orange line) which passed through GPA or NA and cement mortar as
554 displayed in Fig. 3f and Fig. 3i. The boundary between cement mortar and NA could be
555 distinctly identified according to the BSE image and the sudden change of silicon element. In

556 comparison, the interface between cement mortar and GPA was denser than that between the
557 mortar and NA as observed in the BSE image and elemental mapping. As shown in Fig. 3d and
558 Fig. 3g, lower number of micro-cracks with narrow width were found along the GPA-matrix
559 interface compared with the NA-matrix interface, indicating an excellent GPA-matrix bond in
560 GAC. In addition, the element contents at the interface zone between GPA and cement mortar
561 were higher than that between NA and cement mortar (Fig. 3f and Fig. 3i), which could be due
562 to the chemical reaction between GPA and cement mortar [50].

563 **5 Discussion**

564 In this study, red mud (RM) and flue gas residues (FGR) were utilized as partial replacements
565 of common precursors and commercial alkaline activator respectively to synthesize geopolymer
566 aggregates (GPA), aiming to recycle as much industrial wastes as possible into one product. It
567 was found that the geopolymer pastes incorporating RM (40% mass replacement of FA) and
568 FGR (24% or 32% mass substitute of sodium metasilicate) could maintain a similar
569 compressive strength level to the control samples. The lesser identified peaks and lower
570 intensity of some peaks in geopolymer pastes compared with raw RM and FGR from XRD,
571 TGA and FTIR curves as shown in Fig. 1b and Fig. 2(e-i), which revealed that RM and FGR
572 have participated in the geopolymer reaction. Besides, the high alkalinity of RM revealed by
573 the higher first peak in heat evolution curves (Fig. 2c) may also have positive effect on the
574 reaction [11].
575 On the other hand, owing to many kinds of crystal phases existing in RM as shown in Fig. 1b,
576 most of the $SiO_2$ and $Al_2O_3$ in raw RM were difficult to be dissolved. Previous studies have
577 indicated that mechanical activation or thermal or alkali-thermal pre-treatment could improve
578 their dissolution efficiencies [12, 75-78]. However, raw RM was directly used as precursor to
579 save cost in this study. Hence the dissolution degree of $SiO_2$ and $Al_2O_3$ was low. Besides, Fe in
580 raw RM was mainly presented in hematite or octahedral $Fe^{3+}$ form, which were also difficult to
581 participate in gel generation [12, 75]. These unreacted RM particles would act as fillers. Various
582 crystal phases were also detected in FGR as displayed in Fig. 1b and some phases were
583 remained in the produced geopolymer pastes as shown in Fig. 2e. Moreover, the lower peak

584 intensities in FTIR curves also indicated the incomplete participation of $Na_2O$ in FGR. In
585 addition, the dissolution and reaction of RM and FGR demanded time as revealed by the heat
586 evolution rate as plotted in Fig 2(c-d). Moreover, the presence of impurities and heavy metals
587 as described in Section 4.1.6 may also slow down the reaction of RM and FGR in the
588 geopolymer system. It should be mentioned here that despite the incomplete reaction of RM
589 and FGR, their produced geopolymer maintained a comparable performance. In the future, the
590 possibility of increasing the utilization ratio of RM and FGR can be further investigated.
591 As observed from Fig. 3(d-f), although the mechanical property of GPA was comparatively
592 weaker than that of NA, the enhanced aggregate/matrix interaction (due to chemical reaction)
593 in GAC could produce a thick ITZ between GPA and the cementitious matrix. Therefore, a
594 considerable decrease in the strength of GAC was not observed even at 100% replacement level
595 of natural aggregate. The strength/density ratio of GAC was lower than that of NAC. Hence,
596 the structure efficiency of GAC still has space to be improved in future study.

597 **6 Conclusions**

598 This study has confirmed the feasibility and good performance of GPA using RM and FGR as
599 partial substitutes of traditional precursors and commercial activator, respectively. The detailed
600 conclusions are as follows:

601 - Geopolymer pastes produced with 40% mass of FA replaced by RM and 32% $Na_2O$ in
602 commercial activator replaced by FGR showed only a slight decrease in compressive
603 strength.
604 - The reaction mechanism through heat evolution, XRD, TG and FTIR investigations have
605 demonstrated that RM could effectively participate in the chemical reaction along with the
606 nearly complete dissolution of FGR. However, reaction rate of RM and FGR was lower at
607 the early stage.
608 - TCLP and SPLP tests revealed that the leaching concentrations of all measured heavy
609 metals in GPA were far below the limits. The cost and carbon emissions per MPa of GPA
610 in this study were the lowest compared with other GPA in literature.
611 - When GPA were used to prepare concrete, GAC could achieve a similar strength to NAC

and had an improved ITZ compared to NAC as observed by the failure patterns of samples and BSE-EDS analysis. The elastic modulus of GAC did not show significant changes when replacement level of GPA was less than 50% GPA, while it decreased after percentage of GPA was increased over 50%. In the future, the durability properties of GAC should be further studied in the future.

## Conflict of interest

The authors declare that they have no conflict of interest.

## Acknowledgments

The authors would like to acknowledge the financial support received from NSFC/RGC Joint Research Scheme (N_PolyU542/20), Hong Kong RGC General Research Fund (No. 15223120), The Hong Kong Polytechnic University through the Research Centre for Resources Engineering towards Carbon Neutrality (No. BBC7) and the Hong Kong Polytechnic University Ph.D. studentship, awarded to the first author.

## CRediT Author Statement

**LP Qian**: Conceptualization, Methodology, Investigation, Visualization, Writing - Original Draft. **MR Ahmad**: Investigation, Methodology, Validation, Writing - Review & Editing. **JC Lao**: Investigation, Visualization, Writing - Review & Editing. **JG Dai**: Conceptualization, Funding Acquisition, Supervision, Writing - Review & Editing.

## References

[1] C. R. Borra, B. Blanpain, Y. Pontikes, K. Binnemans, and T. Van Gerven, "Smelting of bauxite residue (red mud) in view of iron and selective rare earths recovery," *Journal of Sustainable Metallurgy,* vol. 2, no. 1, pp. 28-37, 2016.

[2] S. Ahmed, T. Meng, and M. Taha, "Utilization of red mud for producing a high strength binder by composition optimization and nano strengthening," *Nanotechnology Reviews,* vol. 9, no. 1, pp. 396-409, 2020.

[3] S. M. A. Qaidi, B. A. Tayeh, H. F. Isleem, A. R. G. de Azevedo, H. U. Ahmed, and W. Emad, "Sustainable utilization of red mud waste (bauxite residue) and slag for the production of geopolymer composites: A review," *Case Studies in Construction Materials,* vol. 16, 2022.

[4] J. He, Y. Jie, J. Zhang, Y. Yu, and G. Zhang, "Synthesis and characterization of red mud and rice husk ash-based geopolymer composites," *Cement and Concrete Composites,* vol. 37, pp. 108-118, 2013.

[5] J. Zhang *et al.*, "Sustainable utilization of bauxite residue (Red Mud) as a road material in pavements: A

critical review," *Construction and Building Materials,* vol. 270, p. 121419, 2021.
[6] Y. Hua, K. V. Heal, and W. Friesl-Hanl, "The use of red mud as an immobiliser for metal/metalloid-contaminated soil: a review," *Journal of hazardous materials,* vol. 325, pp. 17-30, 2017.
[7] E. Mukiza, L. Zhang, X. Liu, and N. Zhang, "Utilization of red mud in road base and subgrade materials: A review," *Resources, Conservation and Recycling,* vol. 141, pp. 187-199, 2019.
[8] M. Wang and X. Liu, "Applications of red mud as an environmental remediation material: A review," *Journal of Hazardous Materials,* vol. 408, p. 124420, 2021.
[9] A. Kumar, T. J. Saravanan, K. Bisht, and K. I. S. A. Kabeer, "A review on the utilization of red mud for the production of geopolymer and alkali activated concrete," *Construction and Building Materials,* vol. 302, p. 124170, 2021.
[10] Y. Sun *et al.*, "Preparation and characteristics of modified red mud-municipal solid waste incineration bottom ash binder," *Journal of Building Engineering,* vol. 46, p. 103760, 2022.
[11] H. Choo, S. Lim, W. Lee, and C. Lee, "Compressive strength of one-part alkali activated fly ash using red mud as alkali supplier," *Construction and Building Materials,* vol. 125, pp. 21-28, 2016.
[12] N. Ye *et al.*, "Transformations of Na, Al, Si and Fe species in red mud during synthesis of one-part geopolymers," *Cement and Concrete Research,* vol. 101, pp. 123-130, 2017.
[13] D. Amutha Rani, A. R. Boccaccini, D. Deegan, and C. R. Cheeseman, "Air pollution control residues from waste incineration: Current UK situation and assessment of alternative technologies," *Waste Management,* vol. 28, no. 11, pp. 2279-2292, 2008.
[14] M. J. Quina, J. M. Bordado, and R. M. Quinta-Ferreira, "Recycling of air pollution control residues from municipal solid waste incineration into lightweight aggregates," *Waste management,* vol. 34, no. 2, pp. 430-438, 2014.
[15] A. Białowiec, W. Janczukowicz, Z. M. Gusiatin, A. Thornton, J. Rodziewicz, and M. Zielińska, "Recycling potential of air pollution control residue from sewage sludge thermal treatment as artificial lightweight aggregates," *Waste Management & Research,* vol. 32, no. 3, pp. 221-227, 2014.
[16] A. A. Bogush *et al.*, "Co-processing of raw and washed air pollution control residues from energy-from-waste facilities in the cement kiln," *Journal of Cleaner Production,* vol. 254, p. 119924, 2020.
[17] J. Stegemann, "The potential role of energy-from-waste air pollution control residues in the industrial ecology of cement," *Journal of Sustainable Cement-Based Materials,* vol. 3, no. 2, pp. 111-127, 2014.
[18] M. R. Ahmad, J. Lao, J. G. Dai, D. Xuan, and C. S. Poon, "Upcycling of air pollution control residue waste into cementitious product through geopolymerization technology," *Resources, Conservation and Recycling,* vol. 181, p. 106231, 2022.
[19] S. İpek, O. A. Ayodele, and K. Mermerdaş, "Influence of artificial aggregate on mechanical properties, fracture parameters and bond strength of concretes," *Construction and Building Materials,* vol. 238, p. 117756, 2020.
[20] F. Tajra, M. Abd Elrahman, C. Lehmann, and D. Stephan, "Properties of lightweight concrete made with core-shell structured lightweight aggregate," *Construction and Building Materials,* vol. 205, pp. 39-51, 2019.
[21] F. Colangelo, F. Messina, L. Di Palma, and R. Cioffi, "Recycling of non-metallic automotive shredder residues and coal fly-ash in cold-bonded aggregates for sustainable concrete," *Composites Part B-Engineering,* vol. 116, pp. 46-52, 2017.
[22] E. Güneyisi, M. Gesoglu, H. Ghanim, S. İpek, and I. Taha, "Influence of the artificial lightweight aggregate on fresh properties and compressive strength of the self-compacting mortars," *Construction and Building*

*Materials,* vol. 116, pp. 151-158, 2016.
[23] K. D. Peng, B. T. Huang, L. Y. Xu, R. L. Hu, and J. G. Dai, "Flexural strengthening of reinforced concrete beams using geopolymer-bonded small-diameter CFRP bars," *Engineering Structures,* vol. 256, p. 113992, 2022.
[24] J.-C. Lao, L.-Y. Xu, B.-T. Huang, J.-G. Dai, and S. P. Shah, "Strain-hardening ultra-high-performance geopolymer concrete (UHPGC): Matrix design and effect of steel fibers," *Composites Communications,* vol. 30, p. 101081, 2022.
[25] J. L. Provis, A. Palomo, and C. Shi, "Advances in understanding alkali-activated materials," *Cement and Concrete Research,* vol. 78, pp. 110-125, 2015.
[26] L. P. Qian, L. Y. Xu, Y. Alrefaei, T. Wang, T. Ishida, and J. G. Dai, "Artificial alkali-activated aggregates developed from wastes and by-products: A state-of-the-art review," *Resources, Conservation and Recycling,* vol. 177, p. 105971, 2022.
[27] L. Y. Xu, B. T. Huang, and J. G. Dai, "Development of engineered cementitious composites (ECC) using artificial fine aggregates," *Construction and Building Materials,* vol. 305, p. 124742, 2021.
[28] L. Y. Xu, B. T. Huang, V. C. Li, and J. G. Dai, "High-strength high-ductility Engineered/Strain-Hardening Cementitious Composites (ECC/SHCC) incorporating geopolymer fine aggregates," *Cement and Concrete Composites,* vol. 125, p. 104296, 2022.
[29] L. Y. Xu, B. T. Huang, J. C. Lao, and J. G. Dai, "Tailoring strain-hardening behavior of high-strength Engineered Cementitious Composites (ECC) using hybrid silica sand and artificial geopolymer aggregates," *Materials & Design,* vol. 220, p. 110876, 2022.
[30] L. Y. Xu, B. T. Huang, L. P. Qian, and J. G. Dai, "Enhancing long-term tensile performance of Engineered Cementitious Composites (ECC) using sustainable artificial geopolymer aggregates," *Cement and Concrete Composites,* vol. 133, p. 104676, 2022.
[31] B. T. Huang, J. X. Zhu, K. F. Weng, V. C. Li, and J. G. Dai, "Ultra-high-strength engineered/strain-hardening cementitious composites (ECC/SHCC): Material design and effect of fiber hybridization," *Cement and Concrete Composites,* vol. 129, p. 104464, 2022.
[32] L. Y. Xu, L. P. Qian, B. T. Huang, and J. G. Dai, "Development of artificial one-part geopolymer lightweight aggregates by crushing technique," *Journal of Cleaner Production,* vol. 315, p. 128200, 2021.
[33] H. M. Zhu Pinghua, Liu Hui, Wang Xinjie, and Chen Chunhong, "Interfacial evaluation of geopolymer mortar prepared with recycled geopolymer fine aggregates," *Construction and Building Materials,* vol. 259 p. 119849, 2020.
[34] A. A. Mesgaria S., Xiao J.Z., "Recycled geopolymer aggregates as coarse aggregates for Portland cement concrete and geopolymer concrete: Effects on mechanical properties," *Construction and Building Materials,* vol. 236, p. 117571, 2020.
[35] *Standard Specification for Coal Fly Ash and Raw or Calcined Natural Pozzolan for Use in Concrete*, 2019.
[36] M. A. Tanakorn Phoo-ngernkham., Mishima Naoki., Hatanaka Shigemitsu., and Chindaprasirt Prinya, "Effects of sodium hydroxide and sodium silicate solutions on compressive and shear bond strengths of FA–GBFS geopolymer," *Construction and Building Materials* vol. 91, pp. 1-8, 2015.
[37] Y. Ke *et al.*, "A zero-waste strategy to synthesize geopolymer from iron-recovered Bayer red mud combined with fly ash: Roles of Fe, Al and Si," *Construction and Building Materials,* vol. 322, 2022.
[38] *Standard Test Method for Compressive Strength of Hydraulic Cement Mortars*, ASTM C109/C109M, 2013.

[39] *Toxicity Characterization Leaching Procedure (TCLP)*, EPA Method 1311, 1992.
[40] *Synthetic Precipitation Leaching Procedure (SPLP)*, EPA Method 1312, 1994.
[41] Y. Maierdan, K. Gu, B. Chen, M. A. Haque, Y. Zhang, and L. Zhao, "Recycling of heavy metal contaminated river sludge into unfired green bricks: Strength, water resistance, and heavy metals leaching behavior – A laboratory simulation study," *Journal of Cleaner Production,* vol. 342, p. 130882, 2022.
[42] *BS EN 933-4. Tests for Geometrical Properties of Aggregates Part 4: Determination of Particle Shape - Shape Index*, 2009.
[43] *Lightweight Aggregates and its Test Methods-Part 2: Test Methods for Lightweight Aggregates*, GB/T 17431.2-2010, 2010.
[44] *Lightweight Aggregates*, UNI EN 13055, 2016.
[45] *BS EN 12350-2. Testing fresh concrete part 2: Slump-test*, 2009.
[46] *Standard Test Method for Compressive Strength of Cylindrical Concrete Specimens*, ASTM C39/C39M-20, 2020.
[47] *Standard Test Method for Static Modulus of Elasticity and Poisson's Ratio of Concrete in Compression*, ASTM C469/C469M-14, 2014.
[48] J. Wang, J. Xie, C. Wang, J. Zhao, F. Liu, and C. Fang, "Study on the optimum initial curing condition for fly ash and GGBS based geopolymer recycled aggregate concrete," *Construction and Building Materials,* vol. 247, p. 118540, 2020.
[49] M. Tuyan, Ö. Andiç-Çakir, and K. Ramyar, "Effect of alkali activator concentration and curing condition on strength and microstructure of waste clay brick powder-based geopolymer," *Composites Part B: Engineering,* vol. 135, pp. 242-252, 2018.
[50] L. P. Qian, Y. S. Wang, Y. Alrefaei, and J. G. Dai, "Experimental study on full-volume fly ash geopolymer mortars: Sintered fly ash versus sand as fine aggregates," *Journal of Cleaner Production,* p. 121445, 2020.
[51] A. Kumar and S. Kumar, "Development of paving blocks from synergistic use of red mud and fly ash using geopolymerization," *Construction and Building Materials,* vol. 38, pp. 865-871, 2013.
[52] Q. Li, H. Xu, F. Li, P. Li, L. Shen, and J. Zhai, "Synthesis of geopolymer composites from blends of CFBC fly and bottom ashes," *Fuel,* vol. 97, pp. 366-372, 2012.
[53] H. Xu, W. Gong, L. Syltebo, K. Izzo, W. Lutze, and I. L. Pegg, "Effect of blast furnace slag grades on fly ash based geopolymer waste forms," *Fuel,* vol. 133, pp. 332-340, 2014.
[54] Y. Alrefaei, Y. S. Wang, J. G. Dai, and Q. F. Xu, "Effect of superplasticizers on properties of one-part Ca(OH)2/Na2SO4 activated geopolymer pastes," *Construction and Building Materials,* vol. 241, p. 117990, 2020.
[55] N. Wang, X. Sun, Q. Zhao, Y. Yang, and P. Wang, "Leachability and adverse effects of coal fly ash: A review," *Journal of Hazardous Materials,* vol. 396, p. 122725, 2020.
[56] X. Zhu, M. Zhang, K. Yang, L. Yu, and C. Yang, "Setting behaviours and early-age microstructures of alkali-activated ground granulated blast furnace slag (GGBS) from different regions in China," *Cement and Concrete Composites,* vol. 114, p. 103782, 2020.
[57] N. I. Bento, P. S. C. Santos, T. E. de Souza, L. C. A. Oliveira, and C. S. Castro, "Composites based on PET and red mud residues as catalyst for organic removal from water," *Journal of Hazardous Materials,* vol. 314, pp. 304-311, 2016.
[58] S. Y. Kim, Y. Jun, D. Jeon, and J. E. Oh, "Synthesis of structural binder for red brick production based on red mud and fly ash activated using $Ca(OH)_2$ and $Na_2CO_3$," *Construction and Building Materials,* vol. 147, pp.

101-116, 2017.
[59] Z. Yang, S. Tian, R. Ji, L. Liu, X. Wang, and Z. Zhang, "Effect of water-washing on the co-removal of chlorine and heavy metals in air pollution control residue from MSW incineration," *Waste Management,* vol. 68, pp. 221-231, 2017.
[60] A. A. Bogush, J. A. Stegemann, and A. Roy, "Changes in composition and lead speciation due to water washing of air pollution control residue from municipal waste incineration," *Journal of Hazardous Materials,* vol. 361, pp. 187-199, 2019.
[61] Z. Yang, R. Mocadlo, M. Zhao, R. D. Sisson, M. Tao, and J. Liang, "Preparation of a geopolymer from red mud slurry and class F fly ash and its behavior at elevated temperatures," *Construction and Building Materials,* vol. 221, pp. 308-317, 2019.
[62] P. Chindaprasirt, S. Thaiwitcharoen, S. Kaewpirom, and U. Rattanasak, "Controlling ettringite formation in FBC fly ash geopolymer concrete," *Cement and Concrete Composites,* vol. 41, pp. 24-28, 2013.
[63] A. Bouaissi, L.-y. Li, M. M. Al Bakri Abdullah, and Q.-B. Bui, "Mechanical properties and microstructure analysis of FA-GGBS-HMNS based geopolymer concrete," *Construction and Building Materials,* vol. 210, pp. 198-209, 2019.
[64] S. Singh, M. Aswath, R. J. c. Ranganath, and b. materials, "Effect of mechanical activation of red mud on the strength of geopolymer binder," vol. 177, pp. 91-101, 2018.
[65] J. K. Prusty and B. Pradhan, "Multi-response optimization using Taguchi-Grey relational analysis for composition of fly ash-ground granulated blast furnace slag based geopolymer concrete," *Construction and Building Materials,* vol. 241, p. 118049, 2020.
[66] A. Rafeet, R. Vinai, M. Soutsos, and W. Sha, "Effects of slag substitution on physical and mechanical properties of fly ash-based alkali activated binders (AABs)," *Cement and Concrete Research,* vol. 122, pp. 118-135, 2019.
[67] *Characteristics Introduction and Regulatory Definitions, Test Methods for Evaluating Solid Waste, Physical/Chemical Methods (SW 846)*, 2004.
[68] M. Xia *et al.*, "Solidification/stabilization of lead-zinc smelting slag in composite based geopolymer," *Journal of Cleaner Production,* vol. 209, pp. 1206-1215, 2019.
[69] L. P. Qian, Y. S. Wang, Y. Alrefaei, and J. G. Dai, "Experimental study on full-volume fly ash geopolymer mortars: Sintered fly ash versus sand as fine aggregates," *Journal of Cleaner Production,* vol. 263, 2020.
[70] A. Castel, S. Foster, T. Ng, J. Sanjayan, R. J. M. Gilbert, and Structures, "Creep and drying shrinkage of a blended slag and low calcium fly ash geopolymer Concrete," vol. 49, no. 5, pp. 1619-1628, 2016.
[71] F. Colangelo and R. Cioffi, "Use of Cement Kiln Dust, Blast Furnace Slag and Marble Sludge in the Manufacture of Sustainable Artificial Aggregates by Means of Cold Bonding Pelletization," *Materials,* vol. 6, no. 8, pp. 3139-3159, 2013.
[72] F. Colangelo, F. Messina, and R. Cioffi, "Recycling of MSWI fly ash by means of cementitious double step cold bonding pelletization: Technological assessment for the production of lightweight artificial aggregates," *Journal of Hazardous Materials,* vol. 299, pp. 181-191, 2015.
[73] Y. Fang, Ahmad Riaz Muhammad, Lao Jian-Cong, Qian Lan-Ping, and Dai Jian-Guo "Development of artificial geopolymer aggregates with thermal energy storage capacity," *Cement and Concrete Composites,* vol. 135, p. 104834, 2023.
[74] P. Ren, T.-C. Ling, and K. H. Mo, "Recent Advances in Artificial Aggregate Production," *Journal of Cleaner Production,* p. 125215, 2020.

[75] Y. Hu *et al.*, "Role of Fe species in geopolymer synthesized from alkali-thermal pretreated Fe-rich Bayer red mud," *Construction and Building Materials,* vol. 200, pp. 398-407, 2019.
[76] S. Singh, M. U. Aswath, and R. V. Ranganath, "Effect of mechanical activation of red mud on the strength of geopolymer binder," *Construction and Building Materials,* vol. 177, pp. 91-101, 2018.
[77] N. Ye *et al.*, "Synthesis and strength optimization of one-part geopolymer based on red mud," *Construction and Building Materials,* vol. 111, pp. 317-325, 2016.
[78] Y. Li, X. Min, Y. Ke, D. Liu, and C. Tang, "Preparation of red mud-based geopolymer materials from MSWI fly ash and red mud by mechanical activation," *Waste Management,* vol. 83, pp. 202-208, 2019.